Supplement of Geochronology, 7, 289–308, 2025
https://doi.org/10.5194/gchron-7-289-2025-supplement

Supplement of

Further investigations into the accuracy of infrared radiofluorescence (IR-RF) and its inter-comparison with infrared photoluminescence (IRPL) dating

Mariana Sontag-González et al.

Correspondence to: Mariana Sontag-González (mariana.sontag-gonzalez@geogr.uni-giessen.de)

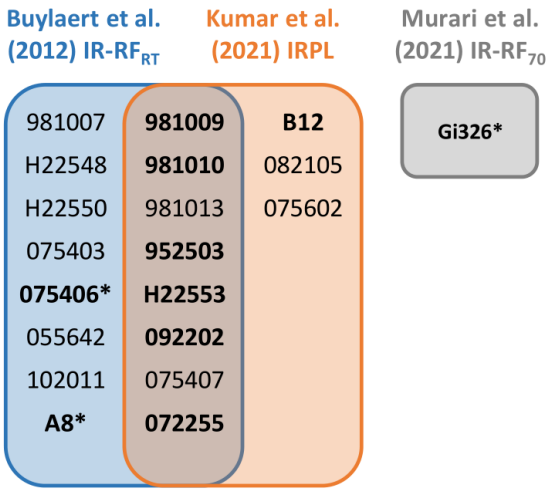

Figure S1: *Overview of discussed samples and previous studies. The ten sample names shown in bold type were measured via IR-RF$_{70}$ in the present work. The three samples marked with an asterisk were measured with a multi-step IRPL protocol in the present work. Measurements of the sixteen samples from Buylaert et al. (2012) were re-analysed here. Note that these partially overlap with the samples measured by Kumar et al. (2021).*

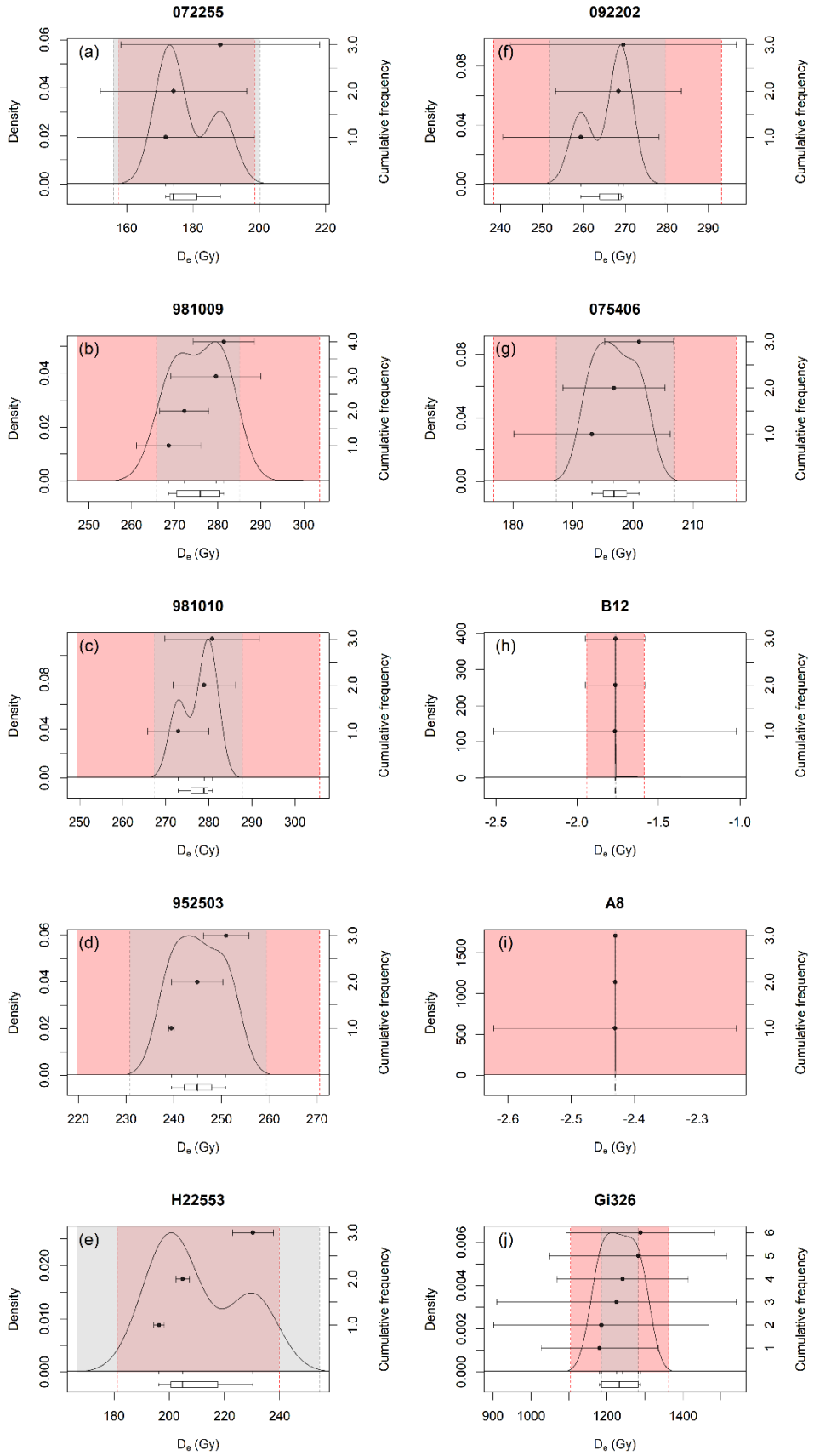

Figure S2: *Kernel density estimate plots of IR-RF$_{70}$ D_e distributions using a segment of the natural dose curve spanning ca. 2–301 Gy and a bandpass filter centred at 850 nm (FWHM: 40 nm). The error bars of individual aliquots include the vertical sliding algorithm error. The red shaded areas indicate two standard errors of the mean D_e. The grey shaded areas indicate the 95% confidence interval of the mean D_e, assuming a Student's t-distribution.*

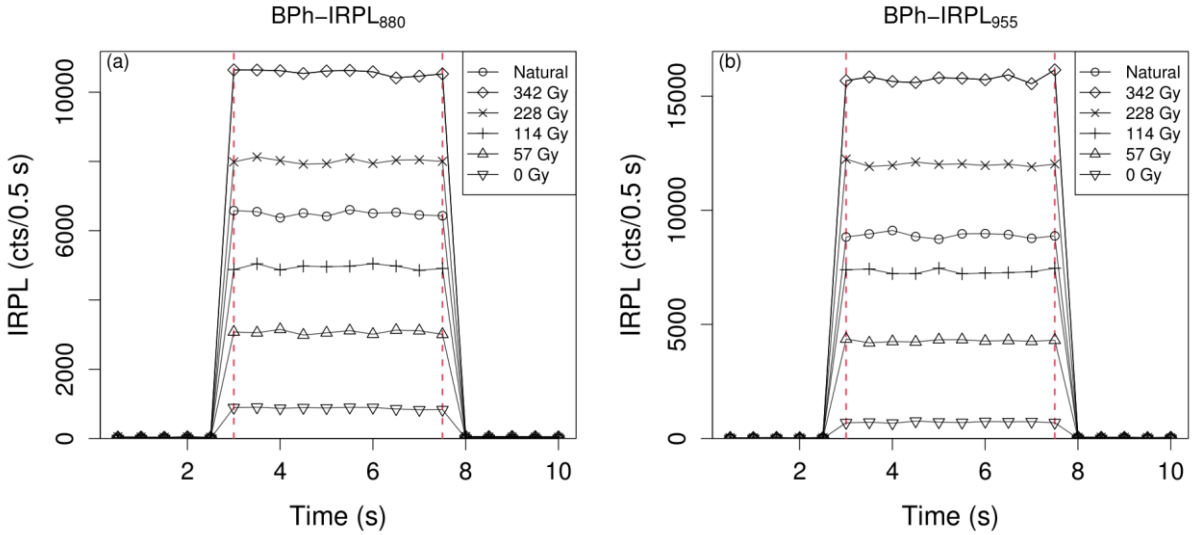

Figure S3: *Example of IRPL curves from (a) step 1 (880 nm emission before preheat) and (b) step 2 (955 nm emission before preheat) for each cycle of the protocol in Table S1 for one aliquot of sample 075406. The red dashed vertical lines denote the integration limits used to calculate the IRPL before preheat (BPh).*

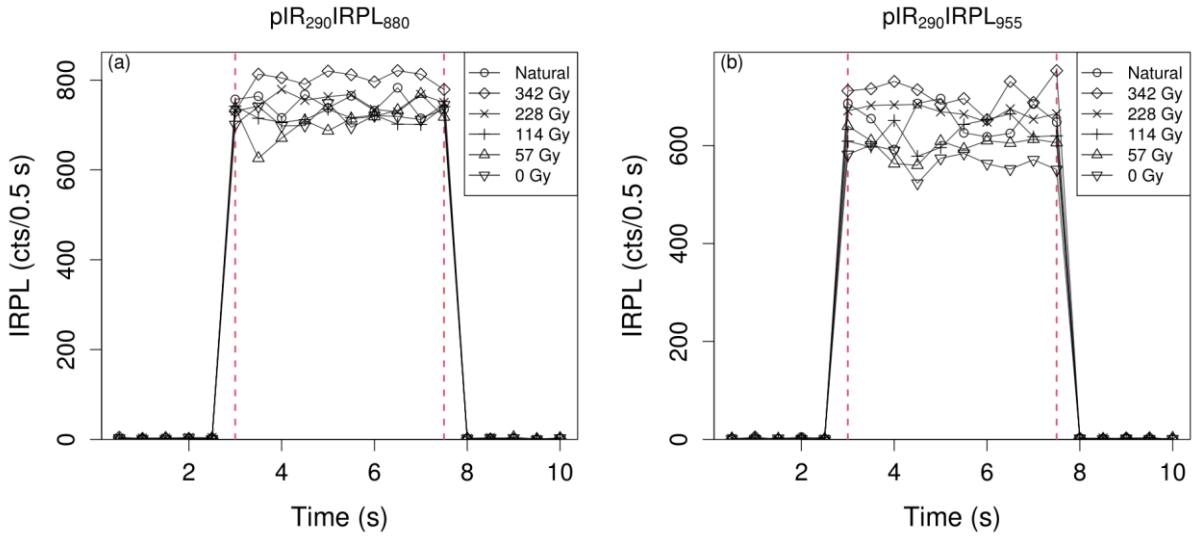

Figure S4: *Example of IRPL curves from (a) step 16 (880 nm emission) and (b) step 17 (955 nm emission) for each cycle of the protocol in Table S1 for one aliquot of sample 075406. The red dashed vertical lines denote the integration limits used to calculate the background IRPL (same aliquot as in Fig. S3).*

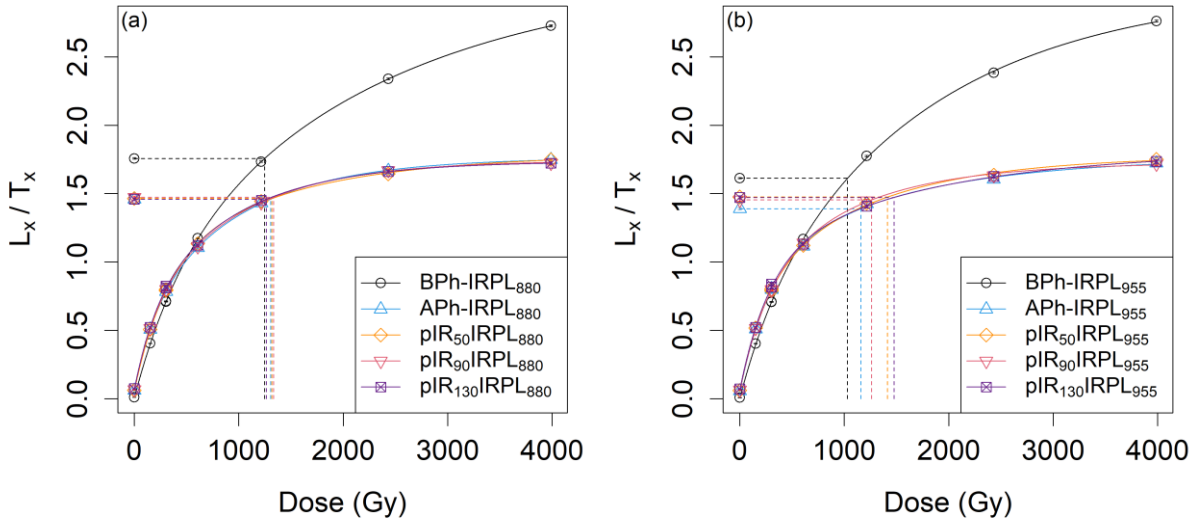

Figure S5: *Examples of dose response curves for the five IRPL signals of (a) the 880 nm and (b) the 955 nm emission. The continuous lines are double exponential functions fitted to the sensitivity corrected signals (L_x/T_x) of one aliquot of sample Gi326. The dashed lines show the interpolation of the natural sensitivity corrected signals (L_n/T_n) onto the fitted curves to yield D_e values.*

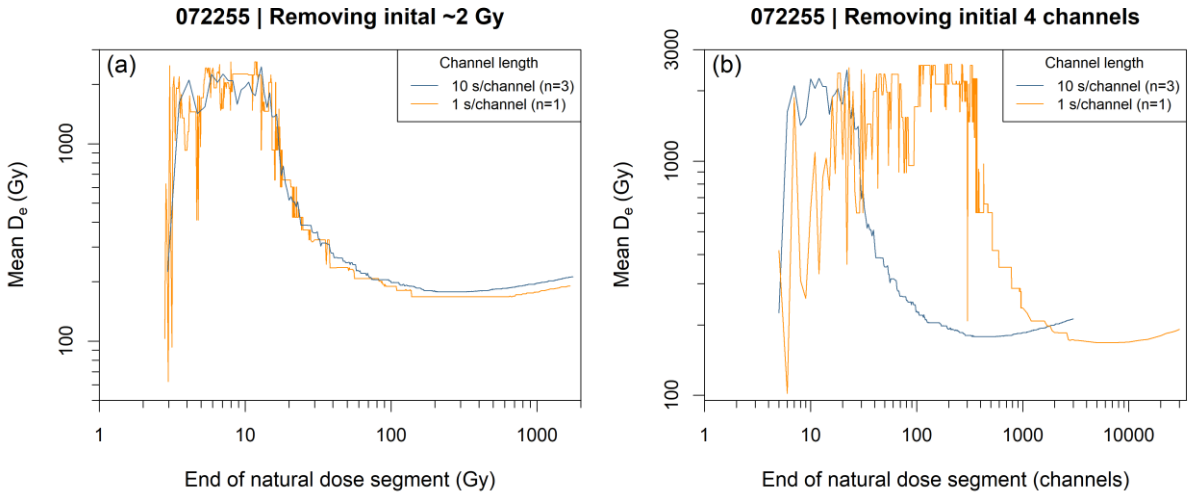

Figure S6: *Effect of channel length on IR-RF$_{70}$ D_e. We re-measured one aliquot of sample 072255 changing the channel length from 10 s to 1 s as a proxy to running the sequence on a reader with a dose rate 10x lower. Note that the mean D_e follows the same pattern when looking at the dose (panel a), but not so when looking only at the channels (panel b), suggesting that the cause of the pattern is a dose-dependent characteristic.*

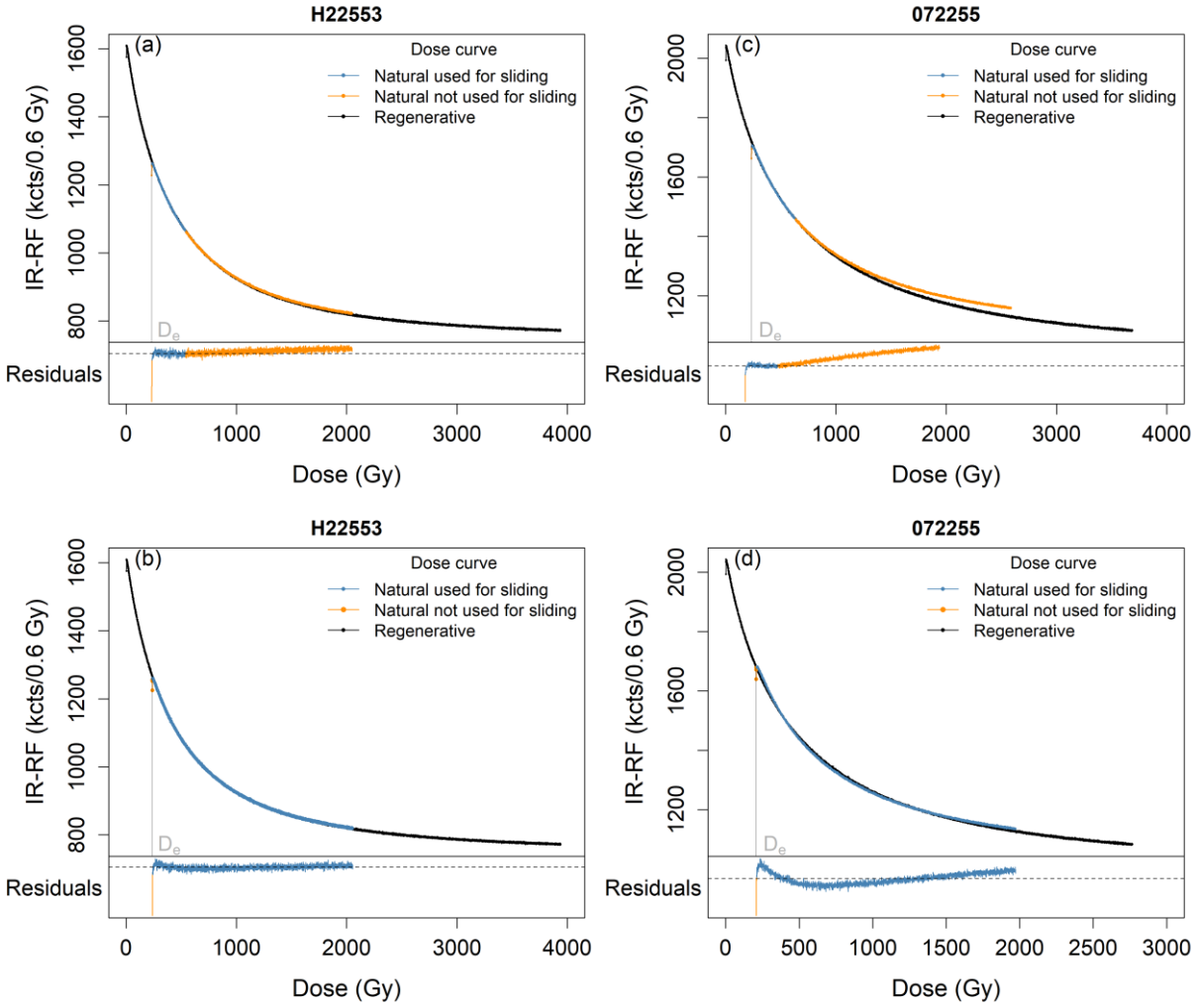

Figure S7: *IR-RF$_{70}$ D_e estimation with a bandpass filter centred at 850 nm (FWHM: 40 nm) using a segment of the natural dose curve spanning either (a, c) 2–301 Gy or (b, d) 2–1808 Gy for one aliquot each of samples (a, b) H22553 and (c, d) 072255. The dashed line in the residual plots indicates zero. Note the poor overall fit quality when using only the shorter segment for sample 072255 (c).*

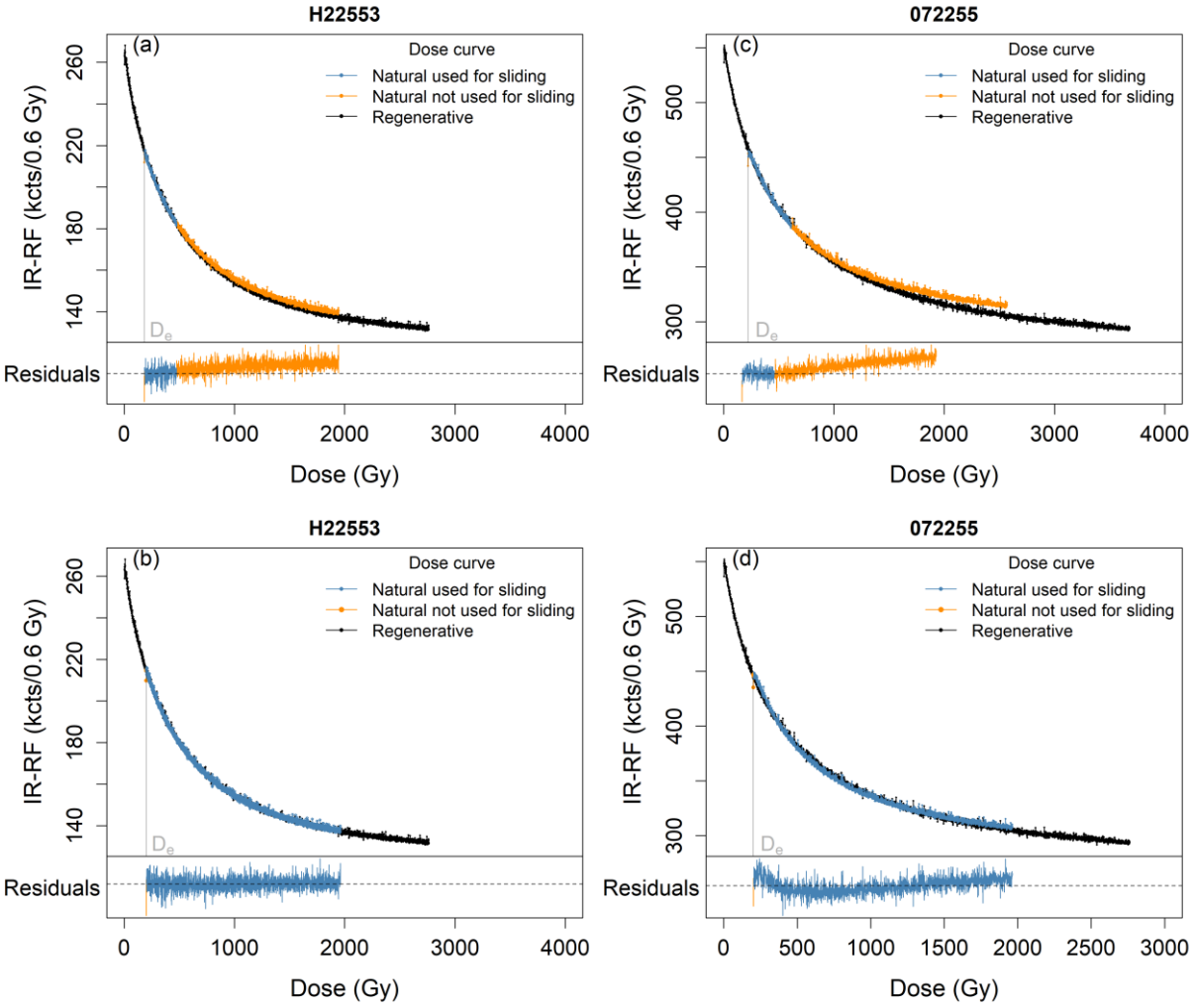

Figure S8: *IR-RF$_{70}$ D_e estimation with a bandpass filter centred at 880 nm (FWHM: 10 nm) using a segment of the natural dose curve spanning either (a, c) 2–294 Gy or (b, d) ca. 2–1763 Gy for one aliquot each of samples (a, b) H22553 and (c, d) 072255. The dashed line in the residual plots indicates zero. Note the poor overall fit quality when using only the shorter segment for sample 072255 (c).*

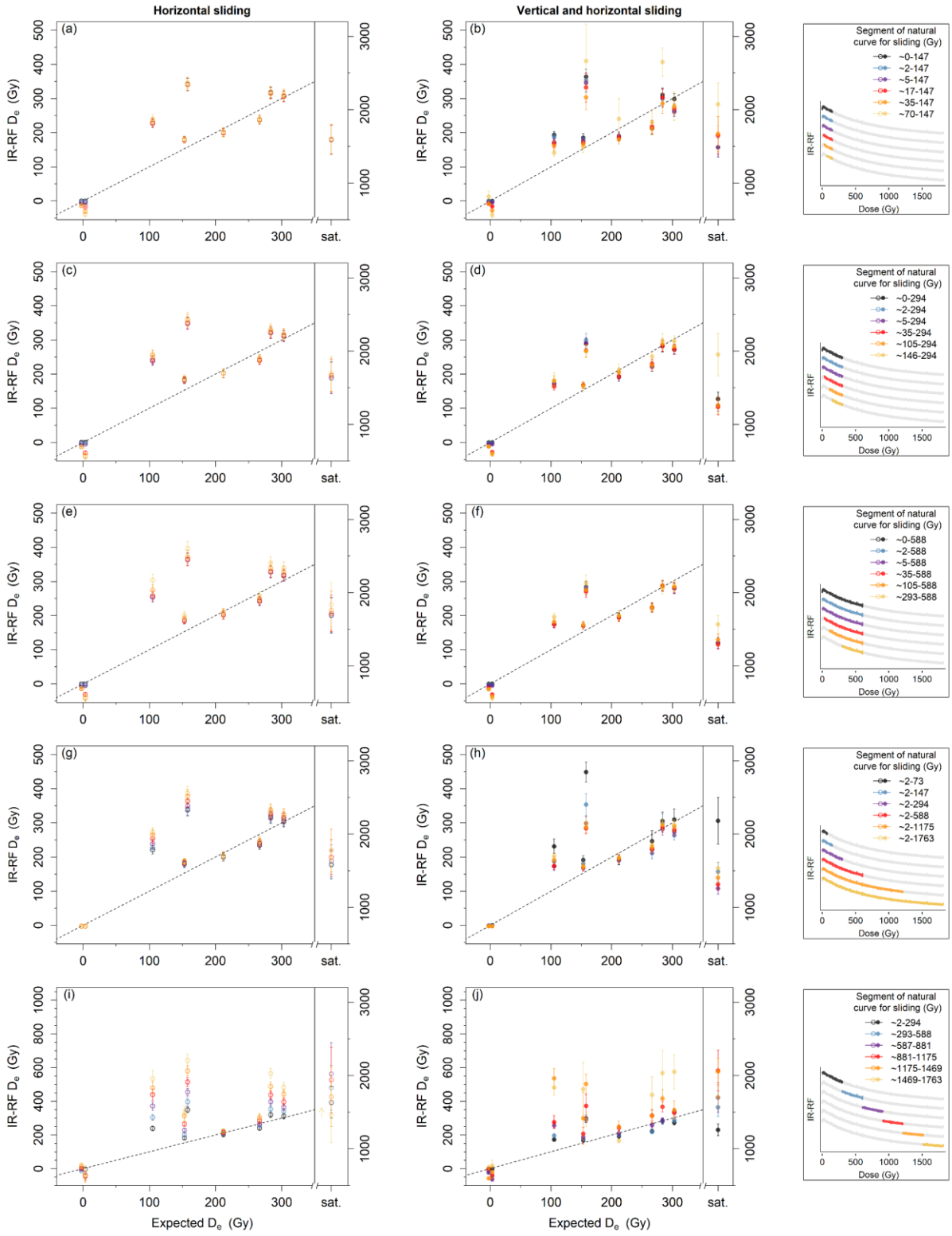

Figure S9: *Comparison of IR-RF$_{70}$ mean D_e values with a filter centred at 880 nm (FWHM: 10 nm) using fixed segments of the natural dose curve and (a, c, e, g, i) only horizontal sliding or (b, d, f, h, j) vertical and horizontal sliding. For clarity, the used segments of a representative natural dose curve (sample 092202) are shown in the legend box to the right of the corresponding plots. Note that a 5 Gy interval was placed between the expected doses of the two modern samples to aid visualization. The D_e for the field-saturated sample Gi326 is shown on the right-hand y-axis in each plot; its expected D_e is 'saturated' (sat.). The dashed line indicates the 1:1 line. (g) Arrows indicate a minimum estimate caused by the limit of the regenerative dose curve.*

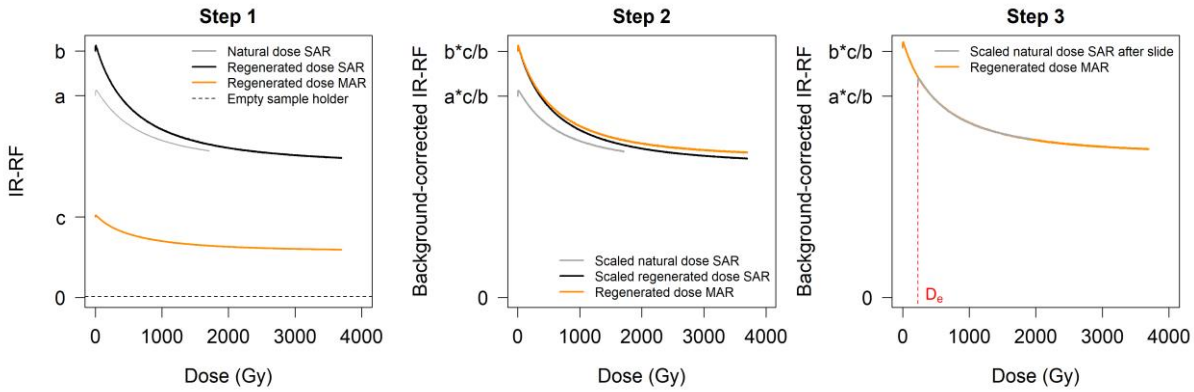

Figure S10: *Schematic of MAR normalisation. After the SAR and MAR measurements (step 1), the natural dose curve of the SAR measurement is normalised (step 2) by dividing every data point by the initial signal intensity of the SAR regenerated dose curve and then multiplying by the initial signal intensity of the MAR regenerated dose curve. The mean signal intensity of an empty sample holder is subtracted as instrumental background from each curve prior to the normalisation. After normalisation, the MAR and SAR regenerated dose curves have the same initial signal intensity and the scaled natural dose (SAR) can be compared with the MAR curve through vertical and horizontal sliding to obtain a* D_e *value (step 3).*

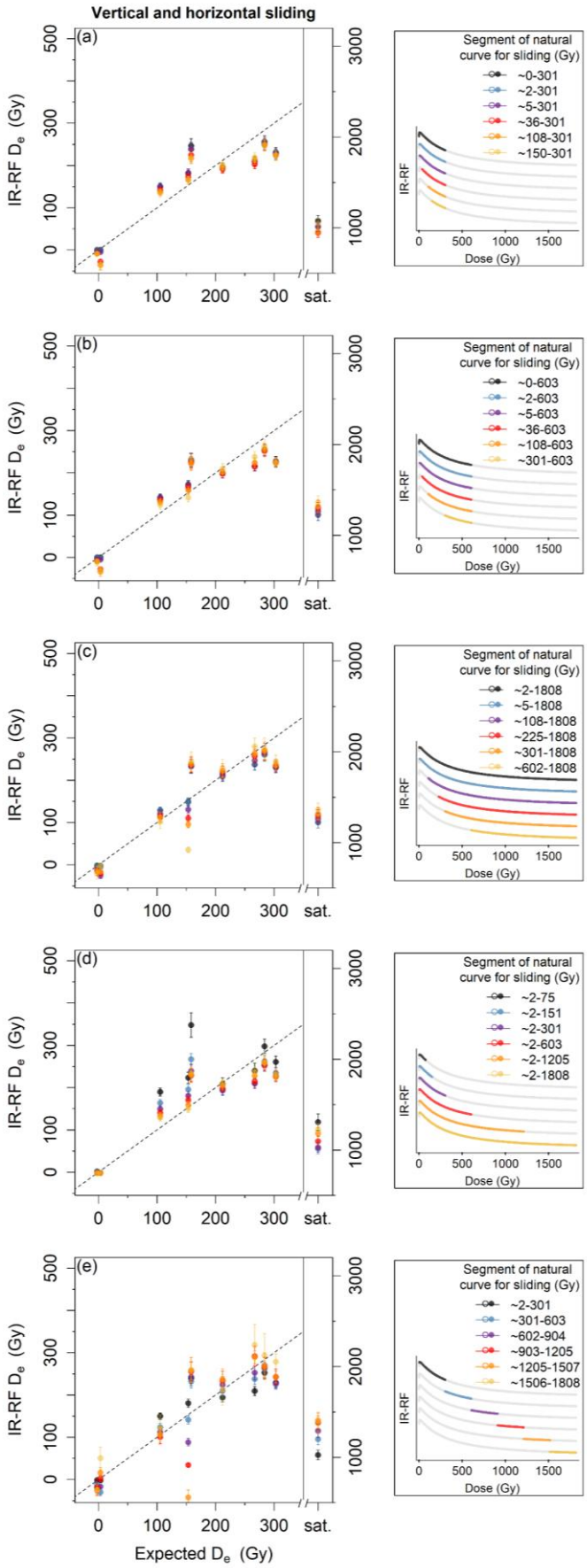

Figure S11: *Comparison of IR-RF$_{70}$ mean D_e values using fixed segments of the natural dose curve with a MAR protocol. For clarity, the used segments of a representative natural dose curve (sample 092202) are shown in the legend box to the right of the corresponding plots. Note that a 5 Gy interval was placed between the expected doses of the two modern samples to aid visualization. The D_e for the field-saturated sample Gi326 is shown on the right-hand y-axis in each plot; its expected D_e is 'saturated' (sat.). The dashed line indicates the 1:1 line.*

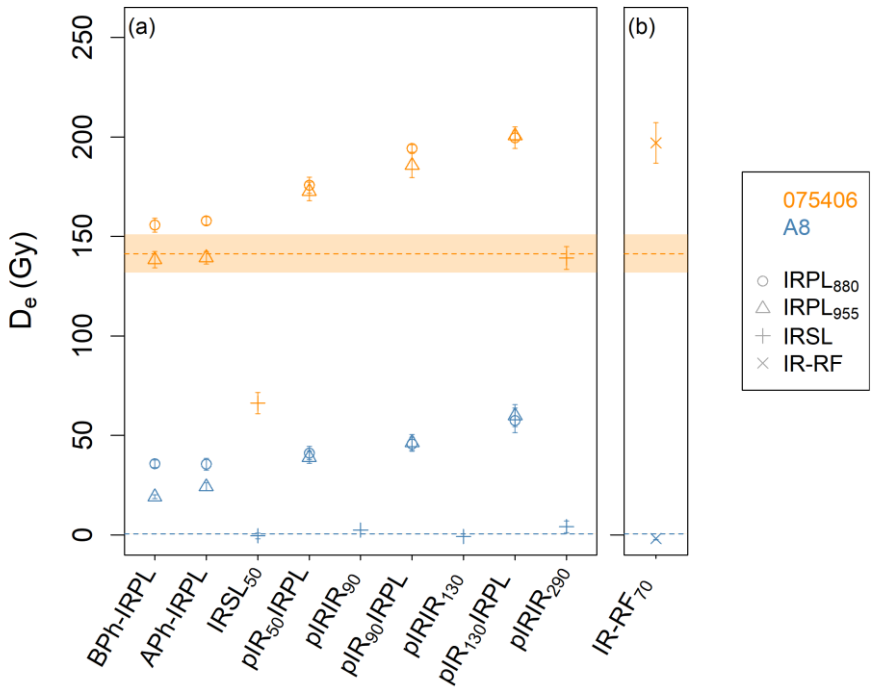

Figure S12: *Mean D_e values obtained for samples 075406 and A8 following (a) the IRPL or (b) the IR-RF_{70} protocols. In panel (a), the x-axis shows the sequential luminescence steps of the IRPL protocol, where BPh and APh stand for before and after the preheat step, respectively. The expected values for the samples are shown as dashed lines with the 1σ uncertainty range shown as shaded regions. For sample 075406, no aliquots were accepted for the $pIRIR_{90}$ nor the $pIRIR_{130}$ signals due to insufficient signal brightness. For sample A8, the same signals delivered only one accepted aliquot out of seven.*

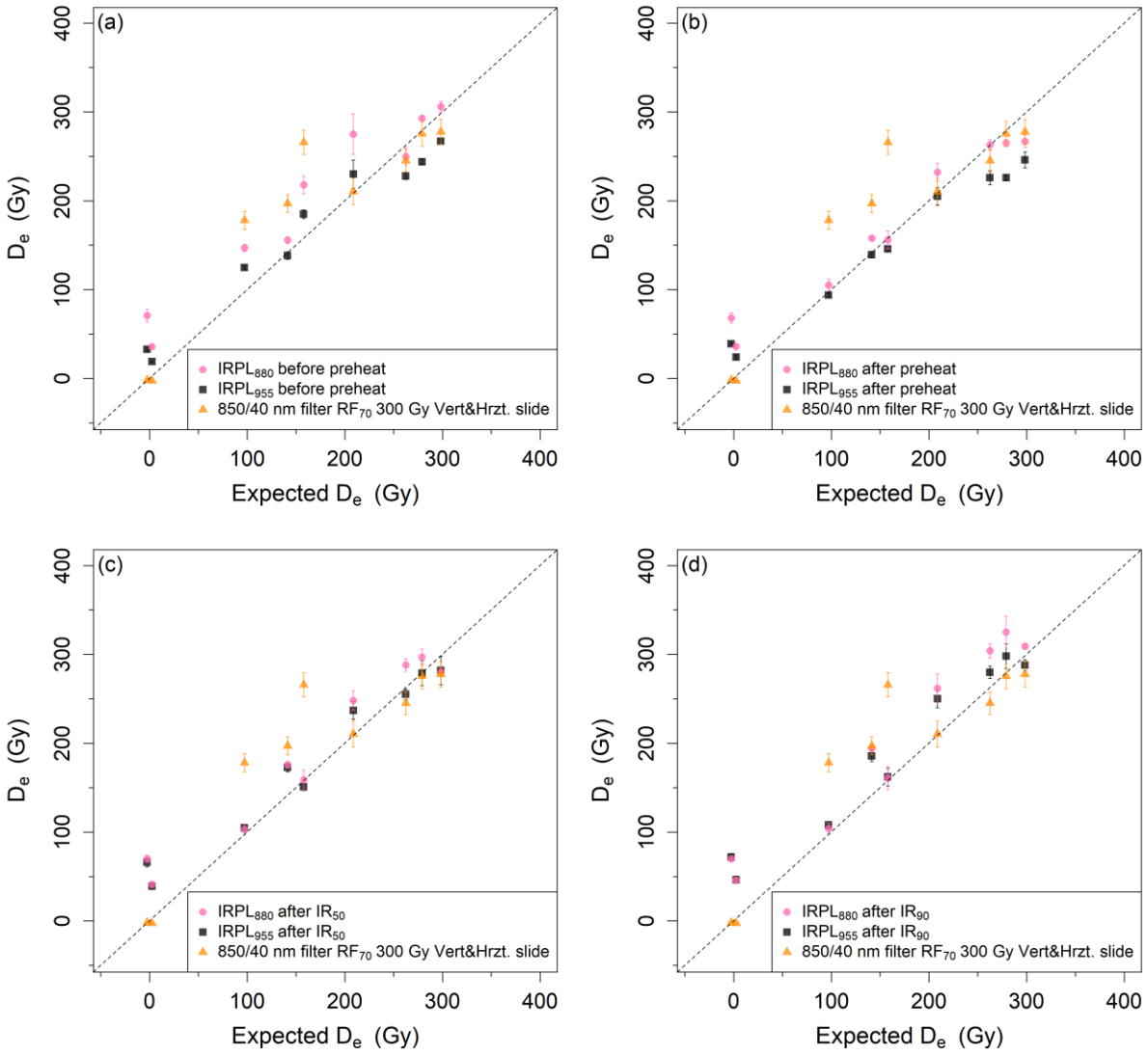

Figure S13: *Comparison of mean IRPL and IR-RF_{70} D_e against their expected values varying the IRPL signals: (a) BPh-IRPL, (b) APh-IRPL, (c) pIR_{50}IRPL, and (d) pIR_{90}IRPL. The IRPL D_e are a combination of new measurements and those from Kumar et al. (2021). The subscript after 'IRPL' in the legend indicates the wavelength of the targeted emission. For RF_{70} D_e estimation, we used a segment of the natural dose curve spanning 600 Gy but rejecting the initial 3 Gy. Note that a 5 Gy interval was placed between the expected doses of the two modern samples to aid visualization.*

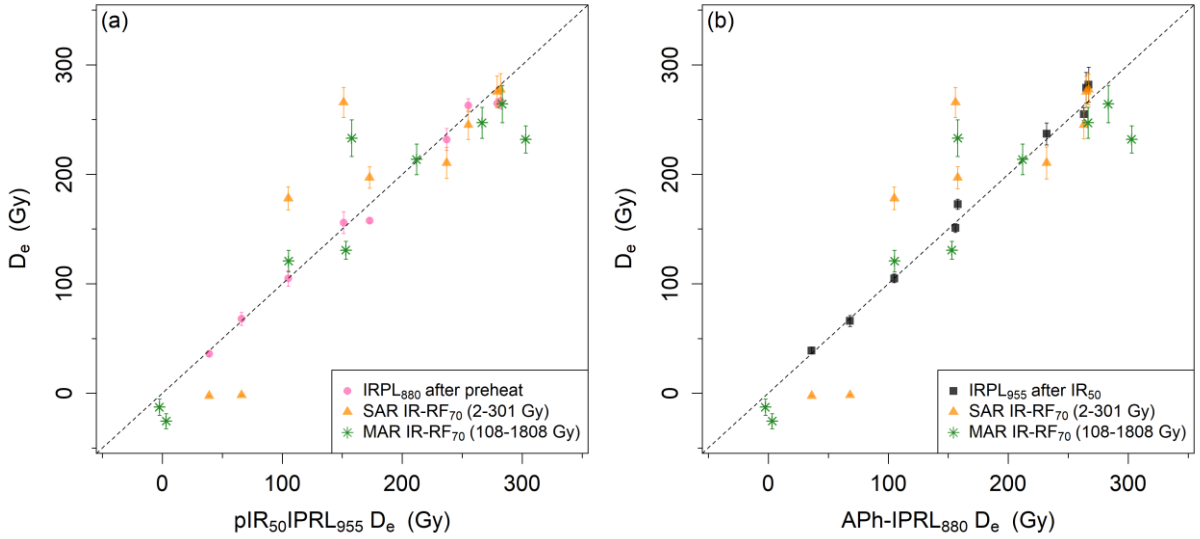

Figure S14: *Comparison of RF_{70} mean D_e values and the best-performing IRPL: (a) $IRPL_{955}$ after IR_{50} and (b) $IRPL_{880}$ after preheat as the x-axis values.*

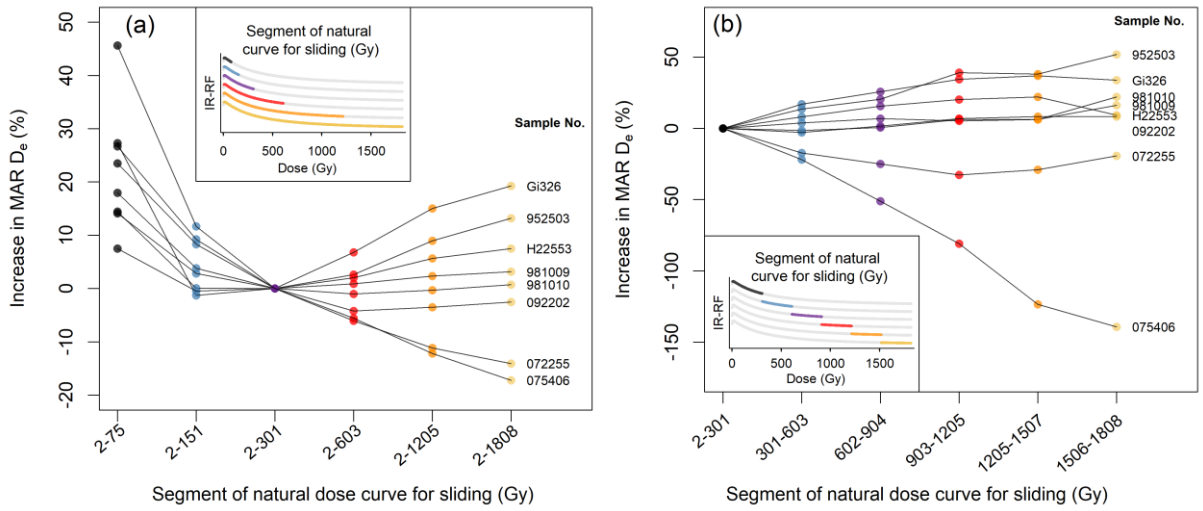

Fig. S15: *Test of progressive sensitivity changes during the MAR IR-RF$_{70}$ natural dose curve measurement. D_e values of non-modern samples were obtained using fixed segments of the natural dose curve according to the x-axis labels with vertical and horizontal sliding (same data and colours as in (a) Fig. S11d and (b) Fig. S11e). The increase in D_e is relative to that obtained from the segment 2−301 Gy.*

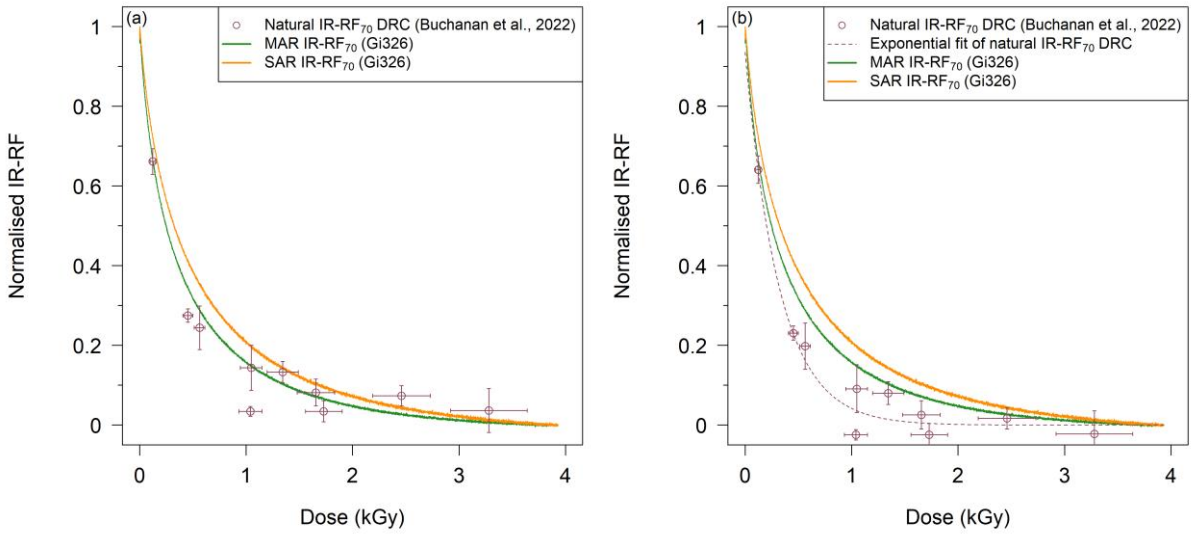

Figure S16: *DRC shape comparison of representative aliquots of Gi326 and a natural IR-RF DRC obtained from samples from the Chinese Loess Plateau (Buchanan et al., 2022). A background was subtracted from the measured IR-RF curves of sample Gi326, corresponding to the median value of the last 100 channels (~60 Gy) before being were normalised to their maximum values. (a) The data points obtained by Buchanan et al. (2022) to create a natural DRC are shown scaled to visually best fit the MAR IR-RF curve. (b) An exponential function was fitted to the data points from Buchanan et al. (2022), subtracting as background the minimum signal value. For better comparison, the fit and the data points are shown normalised to the saturation value of the fit (signal value at 3930 Gy).*

Table S1: *IRPL measurement protocol. BPh and APh refer to before and after preheat, respectively. This sequence is repeated for each natural and regenerative dose point.*

#	Measurement step	Resulting signal
0	Natural or regenerative dose	-
1	$IRPL_{880}$	BPh-$IRPL_{880}$
2	$IRPL_{955}$	BPh-$IRPL_{955}$
3	Preheat at 320°C for 60 s	-
4	$IRPL_{880}$	APh-$IRPL_{880}$
5	$IRPL_{955}$	APh-$IRPL_{955}$
6	IRSL at 50°C for 100 s	$IRSL_{50}$
7	$IRPL_{880}$	pIR_{50} $IRPL_{880}$
8	$IRPL_{955}$	pIR_{50} $IRPL_{955}$
9	IRSL at 90°C for 100 s	$pIR_{50}IR_{90}$
10	$IRPL_{880}$	pIR_{90} $IRPL_{880}$
11	$IRPL_{955}$	pIR_{90} $IRPL_{955}$
12	IRSL at 130°C for 100 s	$pIR_{90}IR_{130}$
13	$IRPL_{880}$	pIR_{130} $IRPL_{880}$
14	$IRPL_{955}$	pIR_{130} $IRPL_{955}$
15	IR cleanout at 290°C for 100 s	pIR_{130} IR_{290}
16	$IRPL_{880}$	background $IRPL_{880}$
17	$IRPL_{955}$	background $IRPL_{955}$
18	Test dose	-
19–35	Repeat steps 1–17	

References

Buchanan, G. R., Tsukamoto, S., Zhang, J., and Long, H.: Testing the natural limits of infrared radiofluorescence dating of the Luochuan loess-palaeosol sequence, Chinese Loess Plateau, Radiat. Meas., 155, 106797, https://doi.org/10.1016/j.radmeas.2022.106797, 2022.

Buylaert, J.-P., Jain, M., Murray, A. S., Thomsen, K. J., and Lapp, T.: IR-RF dating of sand-sized K-feldspar extracts: A test of accuracy, Radiat. Meas., 47, 759–765, https://doi.org/10.1016/j.radmeas.2012.06.021, 2012.

Kumar, R., Kook, M., and Jain, M.: Sediment dating using Infrared Photoluminescence, Quat. Geochronol., 62, 101147, https://doi.org/10.1016/j.quageo.2020.101147, 2021.

Murari, M. K., Kreutzer, S., Frouin, M., Friedrich, J., Lauer, T., Klasen, N., Schmidt, C., Tsukamoto, S., Richter, D., Mercier, N., and Fuchs, M.: Infrared Radiofluorescence (IR-RF) of K-Feldspar: An Interlaboratory Comparison, Geochronometria, 48, 105–120, https://doi.org/10.2478/geochr-2021-0007, 2021.